analytical chemistry

pubs.acs.org/ac Article

Impact of Plasmonic Photothermal Effects on the Reactivity of Au Nanoparticle Modified Graphene Electrodes Visualized Using Scanning Electrochemical Microscopy

Noah B. Schorr, Michael J. Counihan, Rohit Bhargava, and Joaquín Rodríguez-López*

Cite This: *Anal. Chem.* 2020, 92, 3666−3673 Read Online

ACCESS | Metrics & More | Article Recommendations | Supporting Information

ABSTRACT: Atomically thin graphene electrodes enable the modulation of interfacial reactivity by means of underlying substrate effects. Here we show that plasmonic excitation of microscopic arrays composed of 50 nm Au nanoparticles situated underneath a graphene interface results in localized enhancements on the electrochemical readout. We used scanning electrochemical microscopy (SECM) in the feedback and H_2O_2 collection modes to identify the role of the generated plasmons on the electrochemical response. Using electrochemical imaging, supported by finite-element method simulations, we confirmed that a temperature rise of up to ∼30 K was responsible for current enhancements observed for mass transfer- limited reactions. On single-layer graphene (SLG) we observed a shift in the onset of H_2O_2 generation which we traced back to photothermal induced kinetic changes, raising $k^{o\prime}$ from 1.1 × 10^{-8} m/s to 2.2 × 10^{-7} m/s. Thicker 10-layer graphene electrodes displayed only a small kinetic difference with respect to SLG, suggesting that photothermal processes, in contrast to hot carriers, are the main contributor to the observed changes in interfacial reactivity upon illumination. SECM is demonstrated to be a powerful technique for elucidating thermal contributions to reactive enhancements, and presents a convenient platform for studying sublayer and temperature-dependent phenomena over individual sites on electrodes.

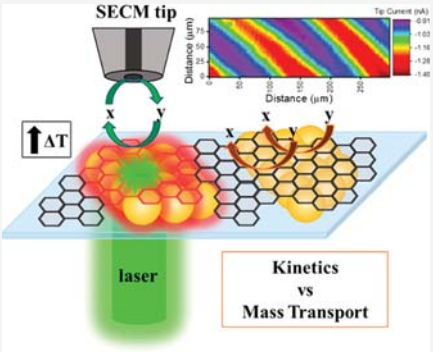

The reactivity and properties of atomically thin 2D materials are strongly influenced by the identity of the underlying substrate.[1−3] Electronic perturbations observable by scanning tunneling microscopy measurements of graphene on copper,[4,5] recently led us to suggest the concept of electrochemically transparent electrodes for inner and outer sphere electron transfer reactions on single layer graphene above noble metals.[6,7] Electronic cooperation between graphene and the substrate opens new avenues for studying effects of sublayer properties on interfacial reactions. The tunable properties of metallic particles based on size and composition make them an attractive material for modulating electrochemical reactivity relative to modifying the 2D material itself, for example, strain engineering.[8]

A characteristic property of metallic nanoparticles is their propensity to generate surface plasmons when excited with light of an appropriate wavelength. These collective oscillations of the particle's conduction band electrons are the basis for techniques like surface-enhanced Raman spectroscopy (SERS), and recent explorations of spontaneous plasmon mediated reactions.[9−13] While examining mechanisms of the oxygen reduction reaction (ORR) on graphene heterointerfaces using our new Raman-scanning electrochemical microscope (SECM) to observe SERS enhancements, we consistently found current increases in SERS active regions. These observations prompted us to explore the enhancements in detail.

The energy imparted during plasmon excitation on the system can be released through either radiative or nonradiative pathways.[14,15] The nonradiative mechanisms include the creation of hot-holes and hot-electrons, along with vibrational collisions that dissipate the energy as heat. These properties have been exploited for various applications, for example, in changing the band gap of semiconductors or for medicinal applications relying on local heating to disrupt cell growth.[16−19] However, due to the multiple pathways of energy dissipation, distinguishing the source responsible for modulating reactivity is not trivial.

When investigating the effects of generated plasmons on reactivity changes, reports in literature commonly propose photothermal processes and hot electron/hole transfer as sources of the observed effects.[11,12,20−22] However, reports do not always agree on the relative role of these two factors: for example, the conversion of 4-nitrobenzenethiol to the amino derivative has been reported as both deriving from photo-

Received: October 17, 2019
Accepted: February 11, 2020
Published: February 11, 2020

thermal effects and not.[22−24] Only recently, studies have sought to determine the relative contributions of these factors.[14,25] This includes the use of SECM by the Willets group for monitoring hot-carrier versus photothermal effects caused by nanoparticle irradiation on photoelectrochemical interfaces.[26] Because SECM is able to quantify site specific electron transfer kinetics,[27,28] and responds to temperature effects at the tip,[29] we turned to this technique to investigate the coupling of graphene with metallic nanoparticles.

Herein, we explore a new avenue of SECM studies of how underlying nanoparticles impact the reactivity of a surface modifying layer for both outer-sphere mediator and inner-sphere electrocatalytic reactions. Expanding the role of nanoparticle-interface interactions and the use of SECM as both a convenient methodology to quantify and spatially resolve contributions of plasmon induced events. By using substrates consisting of gold nanoparticle arrays covered by a continuous sheet of graphene (G-AuNP), we imaged the interplay of underlying nanoparticle contributions to the graphene interfacial reactivity upon laser illumination (Scheme 1). To elucidate the photothermal contributions to the collected signal, we first probed these systems with a redox-mediator. With this information in hand, we also explored O_2 as an electrocatalytic probe by using the collection of H_2O_2 to characterize the impact of underlying plasmons on the oxygen reduction reaction (ORR) kinetics and mechanism. A protective graphene layer also opens avenues for preserving the integrity of nanoparticles throughout electrochemical measurements, additionally providing the opportunity to use plasmonic effects for characterizing the activation parameters of a wide-range of reactions while using SECM.

Scheme 1. SECM Probing of G-AuNP Surface[a]

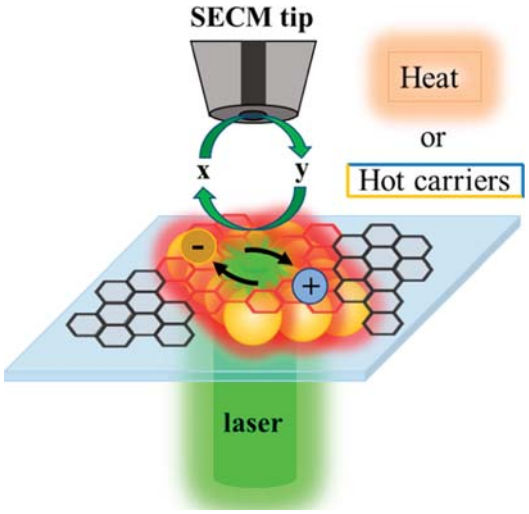

[a]A redox mediator is used to assess current fluctuation due to photothermal or hot carrier processes.

EXPERIMENTAL SECTION

Ten-Layer Graphene Growth. Multilayer graphene was grown on Cu foil using a modified recipe from our previous report.[27] Chemical vapor deposition conditions: atmosphere pressure with no annealing step and growth at 960 °C, 100 sccm Ar, 20 sccm CH_4, and 60 sccm H_2 for 20 min. Single layer graphene was acquired from Grolltex, with batch number 180304-2.

Received graphene and 10-layer graphene had one side covered with 1 layer of 950 K A7 polymethyl merthacrylate (PMMA) via spin-coating at 3000 rpm for 30 s. The protected graphene was floated on top of Cu etchant for 4 h at 41 °C to remove Cu foil. The floating graphene/PMMA sheet went through four rinse steps with DI water, 1 h treatment with 0.1 M EDTA aqueous solution, and four rinse steps with DI water again to fully remove any metal residue.

Nanoparticle Synthesis and Substrate Fabrication. Gold nanoparticles (AuNP) were synthesized in the following fashion. 50 mL of 1 mM $HAuCl_4$ was brought to a boil under stirring. Then 1 mL of 38.8 mM sodium citrate was added to the solution. A color change occurred within 10 s from clear to maroon. Heating was continued for 15 min before removing from heat and continuing to stir for 15 min.

Glass coverslips were silanized with APTMS to attach nanoparticles. Slides were submerged in a 2% APTMS methanol solution for 15 min then thoroughly rinsed with methanol then water before drying under nitrogen. Photolithography was applied to create patterns on the silanized glass slides. A positive photoresist S1813 was spin coated onto graphene at 3000 rpm for 30 s and soft baked at 110 °C for 1.5 min. A contact mask aligner was used to transfer the pattern from the mask to the photoresist layer, creating 50 μm-wide channels separated by 50 μm. After developing in AZ 917 MIF developer for 20 s, the patterned array was created. An aliquot of 100 μL of synthesized AuNPs was dropcast over the patterned region and left for 12 h. The samples were then rinsed with water and dried with nitrogen. Remaining photoresist was removed with acetone and isopropyl alcohol.

A clean graphene/PMMA sheet was transferred onto the glass coverslips with the AuNP arrays and blown dry with argon and dried under vacuum for 12 h. Additional organic solvent treatments were then applied to remove the PMMA protecting layer: 2 h in anisole, 6 h in dichloromethane/acetone mixture (1:1 ratio), and 2 h in isopropanol.

Sample Design. The graphene covered gold nanoparticle arrays (G-AuNP) serve as a template to directly compare subsurface effects on interfacial reactivity. As seen in Figure 1A, the sample surface consists of 50 μm wide arrays, containing a well confined monolayer of ∼50 nm AuNPs (Figure 1B). This pattern allowing discrete analysis of the pristine versus plasmon-affected surface. Alignment of the laser line to the same position as the SECM microelectrode probe ensures that monitoring of the G-AuNP electrochemical performance is localized to the illuminated region. Absorbance of the substrates overlaps with 532 nm laser line (Figure 1C).

Characterization. SEM images were taken with a Hitachi S-4800 high resolution microscope which were obtained at 5−10 kV acceleration voltage and 10 μA emission current. Optical image was taken on a Zeiss Axio Lab.A1 microscope at 50 x magnification. UV−vis spectrum was collected on a HP8542 diode array spectrophotometer.

Electrochemical Tests. All electrochemical measurements were performed in a four-electrode cell configuration conducted using a CHI 920D SECM from CH Instruments (Austin, TX). All potentials in this work are versus the Ag/AgCl reference used for all experiments. For SECM experiments an etched Pt wire (diameter of 11 μm) sealed in glass (Rg = 5) was used as the ultramicroelectrode (UME) probe. An aqueous solution of 1 mM hydroxymethylferrocene

https://dx.doi.org/10.1021/acs.analchem.9b04754
Anal. Chem. 2020, 92, 3666−3673

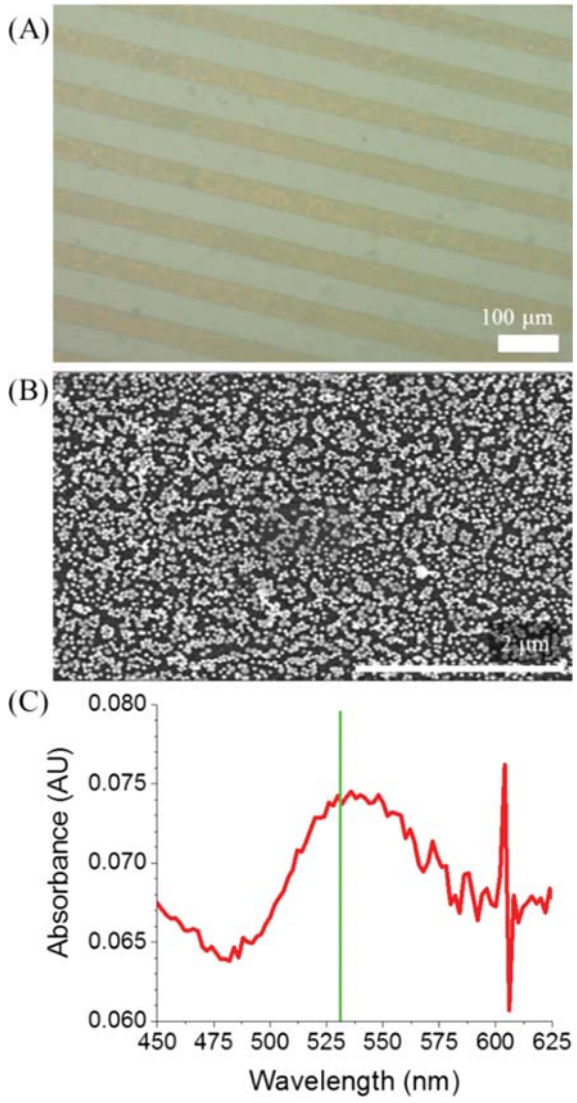

Figure 1. G-AuNP sample. (A) Optical image of G-AuNP. (B) SEM images of G-AuNP. (C) UV−vis of AuNP arrays, green line indicates laser frequency used for experiments.

(FcMeOH) with 100 mM Na_2SO_4 was used for feedback imaging, while an electrolyte solution of 100 mM Na_2SO_4 containing dissolved O_2 from equilibrium with air was used for substrate generation tip collection and oxygen reduction experiments. A Melles Griot 532 nm laser line was focused to a 10 μm spot through an Olympus 50× (N.A. 0.50) objective in an inverse geometry and aligned to the UME location for SECM studies. Laser power was modulated with neutral-density filters. While the presence of pinholes on graphene/metal electrodes is a concern for the measurement of the graphene electrochemical properties,[6,30−32] measurements of outer-sphere and inner-sphere reactions at these type of samples have shown a negligible contribution to their overall electrochemical behavior as measured using SECM.[6,7,27]

Simulations. Simulations were performed using the Transport of Dilute Species (TDS) and Heat Transfer in Fluids (HTF) modules within COMSOL Multiphysics 4.4. For our simulations, we utilized a 2-D axisymmetric geometry representing our UME probe positioned above our extended G-AuNP surface (Supporting Information (SI) Figure S1). Mass transport in the TDS module consisted of diffusion, as described by Fick's first and second laws, and convection, which results from temperature gradients. Since diffusion is a function of temperature and viscosity, coupling to the HTF module consisted on defining the diffusion coefficients for all species through the Stokes−Einstein equation. The viscosity of water as a function of temperature was defined using the expression native to COMSOL Multiphysics, and its thermal conductivity was used as defined in the materials properties available for the program.

Probe currents were modeled with a flux boundary condition on the electrode surface, where flux is based on the Butler−Volmer formalism with the probe biased to a sufficiently high overpotential to achieve mass-transfer limited behavior. These expressions (SI Figure S1) were also functions of local temperature. When modeling positive feedback and substrate generation-tip collection, similar expressions were applied to the substrate electrode, where the substrate has its own associated overpotential and k_f and k_b expressions. Initial concentrations of the species of interest were those used in the experiments.

To model the incident light and resulting photothermal effects, the effective heating spot size was set to 10 μm diameter directly below the probe on the substrate. This portion of the substrate boundary was set at specific temperatures in the HTF module, while the remaining boundaries and solution domain were given the initial value of 298 K.

All simulations modeled chronoamperometric responses at the probe. For SG/TC simulations, the substrate potential was swept linearly with time at 20 mV/s to model the experimental collections. To determine current fluctuations with substrate temperature, the illuminated spot temperature was systematically increased from 298 K, and the steady state currents at the probe after heating were normalized by their values at 298 K to produce i_{on}/i_{off} calibration curves.

RESULTS AND DISCUSSION

Impact of Plasmons on Redox Mediator Electrochemistry. To assess the photothermal effects on the electrochemistry of G-AuNP, we chose the redox mediator hydroxymethylferrocene (FcMeOH) to probe the interface. With the ultramicroelectrode (UME) probe at the surface and biased at an oxidizing potential, and the substrate biased to reduce $FcMeOH^+$ at the mass-transfer limited rate, a positive feedback loop is created between the SECM tip and substrate.[33] Under these conditions, any changes in the current sensed at the probe *should arise from changes in the mass transport of the redox mediator*. When the substrate was biased for positive feedback, but without illumination, no discernible difference across the imaged plane was observed, Figure 2A. The uniform image arises from the fast kinetics of FcMeOH, making differences in the surface conductivity due to underlayer AuNPs unnoticeable. Conversely, as seen in Figure 2B, the array pattern became recognizable once the laser illuminated the G-AuNP.

Because changes in mass transport should be observable further away from the substrate when compared to feedback, we turned to probe approach curves in AuNP regions with and without the laser (Figure 2C). When an approach curve was performed to a biased substrate without laser excitation, positive feedback was seen, typical for conducting materials engaged in rapid redox recycling.[34,35] However, upon

https://dx.doi.org/10.1021/acs.analchem.9b04754
Anal. Chem. 2020, 92, 3666−3673

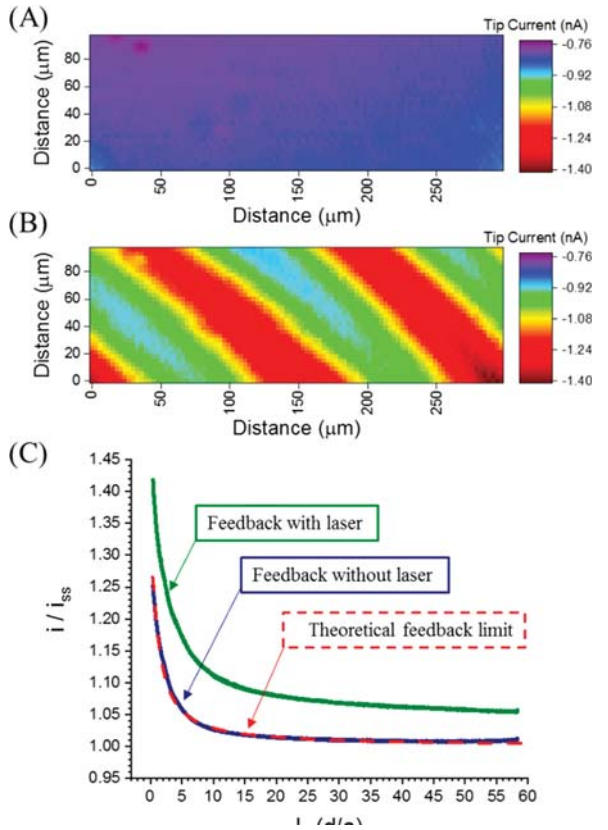

Figure 2. SECM of G-AuNP substrate in the positive feedback mode with FcMeOH. (A) Imaging without laser. (B) Imaging with laser. (C) Approach curves to G-AuNP substrate with and without laser illumination. Red dash line plots theoretical fit for positive feedback conditions. 5.5 μm radius SECM tip held at 0.45 V and substrate at −0.05 V vs Ag/AgCl for feedback experiments.

illumination we observed a positive current shift throughout the approach. Because the substrate is performing at a mass-transfer limitation, the larger current indicates an increase in the mass transport of the mediator between the tip and substrate. In the following sections, we demonstrate that this increase is caused by local solution heating due to photothermal effects from the AuNPs.

Photothermal effects are expected to influence the mass transfer limited current by means of the diffusion coefficient (D),[32]

$$i = 4nFaDC$$

With n being the number of electrons, a the radius of the UME, F is Faraday's constant, and C the concentration of species in solution. The changes D with temperature (T) are expressed through the Einstein-Stokes relationship,

$$D = (k_b T)/(6\pi r\eta(T))$$

where k_b is the Boltzmann constant, r the radius of the species, and $\eta(T)$ is the temperature-dependent solution viscosity.

To correlate the current level at the SECM tip to the local photothermal induced temperature, we measured the changes in current as a function of laser power, shown in Figure 3 as a normalized quantity relating laser on/off states, that is, i_{on}/i_{off}. We sought to understand this behavior with finite-element modeling of the electrochemical system (SI Figure S1). By adjusting the temperature of the illuminated substrate region

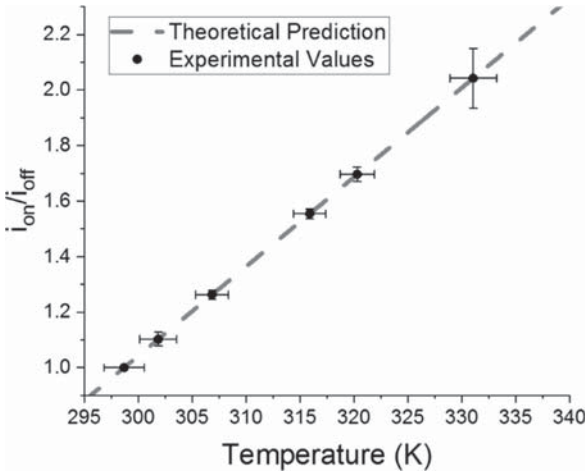

Figure 3. Probing G-AuNP substrate with redox mediator. Gray dashed line shows the simulated i_{on}/i_{off} values for the feedback process. The black points indicate the experimental i_{on}/i_{off} at varying laser powers. 5.5 μm radius SECM tip held at 0.50 V and substrate at −0.15 V vs Ag/AgCl for feedback experiments.

through varying laser power, we established a trend between the temperature induced mass transfer increase and the current of the tip (Figure 3). The experimentally measured current increases and temperature changes calculated from the Einstein-Stokes equation match the linear trend predicted by the simulated model.

The prediction shows very little dependence on the variations in the tip−substrate distance when the heated spot size is larger than 2 μm in radius, which is within the range of the experimental parameters (SI Figure S2). Correlation of the experimental to simulated current increases enables us to create a calibration curve between temperature and laser power. Using the simulated data, we determined that illumination of the nanoparticles caused a temperature increase as large as 33 K as measured by the positive feedback SECM. This temperature increase matches the order of magnitude increase estimated by SERS measurements on nitro-substituted molecules supported on metal nanoparticles and previously established analytical models of plasmonic heating of AuNPs.[23,24,36] In our method, the calculated effects of temperature on reactivity are independent of the presence of plasmonic hot spots, or vibrational signatures of the adsorbed molecules.

ORR at the Graphene/Metal Interface. We next examined how the underlying substrate excitation affects interfacial reactivity for the ORR electrocatalytic reaction. Unlike FcMeOH, which only involves an outer-sphere electron transfer event, the ORR involves multiple electron and proton transfers. There are two main reduction pathways, one leading to the formation of H_2O_2 and the other H_2O; graphitic materials primarily proceed through the former, whereas Pt (the SECM tip disk material) proceeds efficiently through the latter.[37] We have previously shown that underlying Au substrates enhance the reactivity of graphene toward the H_2O_2 forming reaction.[7] SI Figure S3 shows control experiments evaluating mass-transfer effects for the ORR at the Pt tip. These confirmed that laser excitation over G-AuNP areas created a temperature gradient, producing a current enhancement similar to that observed for FcMeOH. Since Pt is one of the best electrocatalysts for the ORR, and thus operates under

https://dx.doi.org/10.1021/acs.analchem.9b04754
Anal. Chem. 2020, 92, 3666−3673

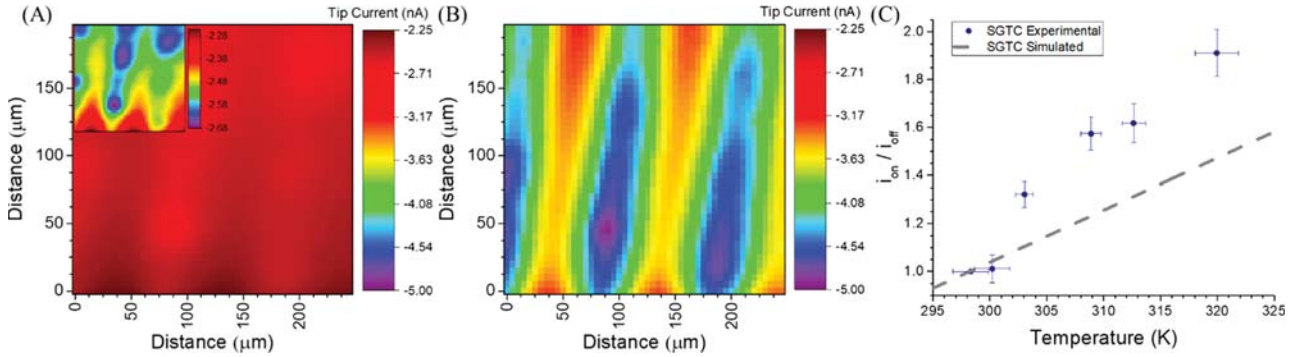

Figure 4. Tip SGTC over G-AuNP surface. (A) Tip SGTC over G-AuNP without laser, using the same current scale as B. Inset shows same image on reduced current scale to highlight location dependent reactivity. (B) Tip SGTC over G-AuNP with laser. (C) Comparison of i_{on}/i_{off} versus temperature for simulated and experimental SGTC. SECM tip held at 1.00 V and substrate at −0.65 V vs Ag/AgCl for SGTC experiments.

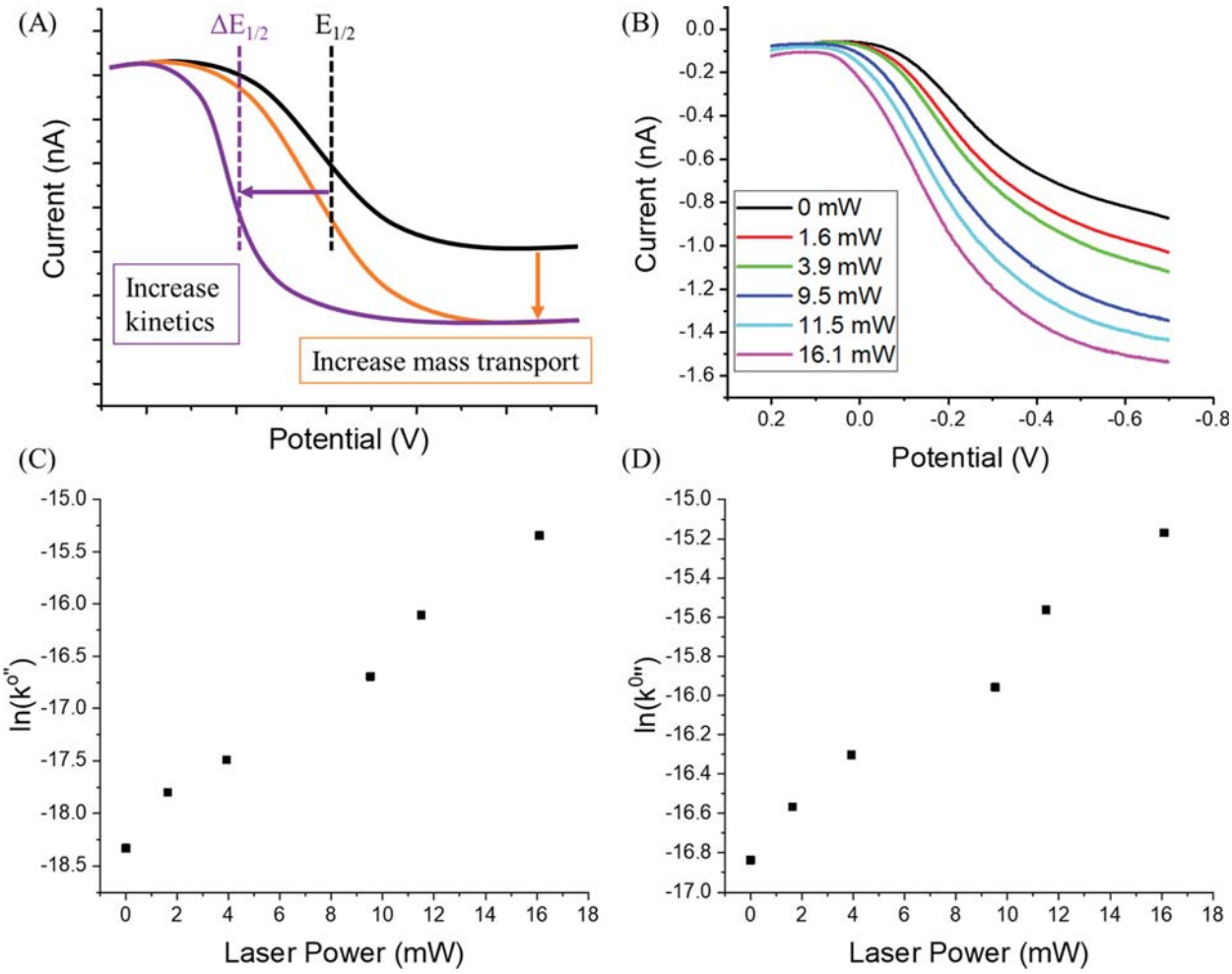

Figure 5. Collection of H_2O_2 at tip during ORR at the substrate. (A) Representation of collection data showing expected response to an increase in diffusion versus an increase in kinetics. (B) Tip current during substrate ORR CV at increasing laser powers. (C) Plot of calculated $k^{o\prime\prime}$ of ORR at the G-AuNP substrate with increasing laser power. (D) Corresponding increase in $k^{o\prime\prime}$ of ORR at the 10-G-AuNP interface with laser power.

mass-transfer limited conditions, this behavior is expected. However, since graphene is a sluggish electrocatalyst for the ORR, the effects of plasmonic excitation could be more profound.

Plasmon generation has been shown to induce doping in graphene via hot carriers, where changes in the graphene band structure is a sought out method for enhancing electrocatalytic reactions.[38,39] To determine the effects of plasmonic excitation we used SECM in the substrate generation tip collection (SGTC) mode to monitor the ORR at the G-AuNP electrode. The substrate was biased to reduce oxygen while the tip was biased at an oxidative potential to collect generated H_2O_2. With the substrate in the dark, the array pattern of the substrate is noticeable, with a higher H_2O_2 production over the

https://dx.doi.org/10.1021/acs.analchem.9b04754
Anal. Chem. 2020, 92, 3666−3673

sublayer AuNPs (Figure 4A). Unlike the case of using the redox mediator FcMeOH, the kinetically more labile inner-sphere ORR reaction greatly depends on the surface structure of the substrate. This is expected as the sublayer nanoparticles causing an increase in generation reactivity at the graphene interface is similar to the case of bulk metals situated beneath graphene.[7] In both cases, graphene acts as a semielectronically transparent layer where the substrate modifies the activation of the interface.[3,5]

Laser illumination allowed once more to visualize differences between modified and unmodified areas, with an average increase in reactivity of ∼200% (Figure 4B). In Figure 4B, the small increase in the background current in the voltammograms in the prewave region as the laser intensity increases is possibly due to the contribution of exposed Au sites (pinholes).[6,7] This is expected since the ORR on Au is activated at a lower overpotential than graphene,[7] but this feature otherwise has a negligible impact in the evaluation of the reaction kinetics at the interface of interest. As seen in Figure 4C a deviating trend emerged between model predictions of H_2O_2 collection enhancements and experimental results. The experimental collection data showed a consistently larger i_{on}/i_{off} value. We hypothesized that discrepancies between these profiles arose from changes in the standard rate constant, k^o. Since these changes are potentially linked to either changes in temperature or generated hot carriers, we set out to explore the corresponding dependencies.

Plasmon Impact on ORR Kinetics. With the SECM tip positioned over a G-AuNP area, we conducted SGTC experiments, that is, SECM tip current vs substrate potential, using cyclic voltammetry (CV). A change in the ORR kinetics was validated by the observation of a lower overpotential to activate the generation of H_2O_2 (Figure 5A). This lowered overpotential is experimentally reflected as a positive shift of the i-E curve for H_2O_2 collection upon illumination. This shift occurs in addition to an increase in current caused by the effects of temperature on diffusion coefficient, as it was described previously for FcMeOH. As seen in Figure 5B, when the SGTC CVs were performed, the collection curves followed the trend expected for an increase both in the k^o and mass transfer. There was no discernible change in the substrate CV (SI Figure S4), which was anticipated given that the portion of the sample irradiated is 4 orders of magnitude smaller than the overall exposed sample area. This highlights the necessity for a site-specific methodology such as SECM for these experiments. The $E_{1/2}$ shift by the G-AuNP seen in Figure 5B is orders of magnitude larger than common potential shifts for electrochemical references at a similar temperature range; it is also[40] four times greater than previously reported for the ORR on illuminated silver nanoparticles supported on top of graphene,[41] and the ORR control experiment at the SECM tip (SI igure S5). Using a rotating ring disk electrode, Schmidt et al. found that a change in temperature between 293 to 333 K the collection of H_2O_2 approximately doubled when performing ORR on single crystal Pt.[42]

The standard rate constant, k^o, is related to temperature and the $E_{1/2}$ by the equation for irreversible kinetics at an electrode operating at steady state,[43] here approximated by the affected spot on the graphene surface probed by the UME,

$$\Delta E_{(1/2)} = R/\alpha F[T'\ln(rk^{o'}/D^{0'}) - T''\ln(rk^{o''}/D^{0''})]$$

$\Delta E_{1/2}$ is the change in half-wave potential, α the transmission coefficient, and R is the ideal gas constant. The T', D_0', $k^{o'}$ are the temperature, diffusion coefficient, and standard rate constant at room temperature, and the double prime represents those at increased temperature values. As seen in Figure 5C, the plot of the natural logarithm of the calculated $k^{o''}$ shows increasing values with increasing laser power. This trend follows the Arrenhius behavior for temperature-dependent kinetics,[44] strongly suggesting that photothermal phenomena are primarily responsible for the 20x increase in the $k^{o'}$ from 1.1×10^{-8} m/s to 2.2×10^{-7} m/s. Graphene layer dependence on AuNP enhancements. To single out hot carrier versus photothermal effects, we explored the dependencies on the number of layers of graphene. Using AuNPs covered by 10-layer graphene (10L-G-AuNP), we conducted SECM measurements with and without laser illumination and compared them to monolayer graphene. The 10L-G-AuNP consisted of the same 50 μm wide AuNP arrays as the G-AuNP, retaining a similar distribution of nanoparticles in the underlayer, with the primary difference being the number of layers of graphene (SI Figure S6). The presence of additional layers separates the gold surface from the electrochemical interface at which molecular oxygen reacts by ∼3.3 nm.[45] We expect that this increased distance reduces the frequency of hot carriers interacting with surface species.[46,47] For example, comparing single layer to 12-layer CVD graphene, Chen et al. found an 80% decrease in carrier diffusion.[48] On the other hand, thermal conductance has found to be of similar magnitudes from single and seven-layer graphene, ∼25 to ∼15 $MWm^{-2}K^{-1}$, respectively, supporting the contention that layer number will not greatly diminish photothermal heating.[49] When performing SGTC, increasing the number of layers of graphene did not block the effects of greater H_2O_2 production over the buried AuNPs (SI Figure S7). Thus, monitoring the potential shift with laser power during SGTC, SI Figure S8, enables a direct comparison of plasmon induced kinetic changes.

Figure 5D evidence that both G-AuNP and 10L-G-AuNP, display very similar dependencies on laser power. Although the overall increase in kinetics is smaller for 10L-G-AuNP (28%), there was only a small difference in the maximum rate between the two substrates caused by the highest intensity laser illumination. The smaller overall increase for the thicker sample is not surprising based on previous studies concluding that multilayer graphene is inherently more reactive than the single layer case.[27,50]

The comparable maximum $k^{o''}$ for the single layer and 10-layer samples alludes to the role of photothermal effects versus hot carriers. If the ORR at the interface was a hot electron-controlled process, it would be expected that the multilayer electrodes would display a significantly smaller effect upon illumination. Conversely, if similar temperatures were achieved at both substrate interfaces, the change in kinetics would be controlled by the photothermal process. The small difference observed between single and 10-layer samples points to the second case. This result, along with the change in rate constant having an Arrhenius dependence, strongly suggests that the ORR on the graphene surface is primarily a function of temperature and not from the creation of hot carriers.

Isolating plasmonic contributions to heterogeneous reactions will never be a trivial pursuit, especially for non-spontaneous reactions, for example, electrochemical catalysis. We intend for this work to serve as a cautionary reference for researches to avoid disregarding the impact of photothermal effects on electron transfer kinetics, and additionally to encourage the use of graphene covered nanoparticles to

https://dx.doi.org/10.1021/acs.analchem.9b04754
Anal. Chem. 2020, 92, 3666−3673

investigate temperature dependent reactions. We envision graphene serving as a versatile template for surface modifications, opening an exciting avenue for temperature dependent reactions on an electrode surface, without the necessity of bulk heating of the electrochemical cell. Finally, the use of nanoparticles affords a wide variety of substrate patterning for site-specific heating to control interfacial reactions.

CONCLUSION

Using multiple modes of SECM in combination with finite-element simulations, we elucidated the role of sublayer gold nanoparticle plasmons on the interfacial reactivity of graphene electrodes. By illuminating the G-AuNP system while monitoring the mass-transfer limited feedback of a redox mediator, photothermal effects were found to increase the surface temperatures by up to ∼30 K. We then turned to the oxygen reduction reaction to probe the impact of plasmons on electrocatalytic performance. A positive shift in the collection of H_2O_2 indicated an increased ORR kinetics with illumination. By varying the laser power intensity, ORR kinetics were found to have an Arrenhius-type dependency, suggesting the photothermal energy dissipation was the main contributor to enhanced electrochemical reactivity.

We further validated this conclusion by conducting experiments on a thicker 10-layer graphene blanket covering the AuNPs, limiting hot carrier interactions with interface species while maintaining similar heat transfer properties. The maximum difference in kinetics was found to be small between the 10- and single layer case, again supporting a photothermal controlled process. While generation of hot carriers may impact some interfacial processes on nanoparticle surfaces, the reactions studied here were predominantly temperature dependent. This opens opportunities for investigations into site-specific temperature dependent reactions using the graphene surface as an atomically thin template for depositing species of interest.

ASSOCIATED CONTENT

Supporting Information

The Supporting Information is available free of charge at https://pubs.acs.org/doi/10.1021/acs.analchem.9b04754.

Geometry and equations used in COMSOL simulations, simulated heating element size and L dependence, SECM results of ORR experiments, mediator imaging experiments, and normalized SGTC curves (PDF)

AUTHOR INFORMATION

Corresponding Author

Joaquín Rodríguez-López − *Department of Chemistry and Beckman Institute for Advanced Science and Technology, University of Illinois at Urbana−Champaign, Urbana, Illinois 61801, United States;* orcid.org/0000-0003-4346-4668; Phone: +1 (217) 300-7354; Email: joaquinr@illinois.edu

Authors

Noah B. Schorr − *Department of Chemistry, University of Illinois at Urbana−Champaign, Urbana, Illinois 61801, United States;* orcid.org/0000-0002-1582-8594

Michael J. Counihan − *Department of Chemistry, University of Illinois at Urbana−Champaign, Urbana, Illinois 61801, United States*

Rohit Bhargava − *Department of Chemistry and Beckman Institute for Advanced Science and Technology, University of Illinois at Urbana−Champaign, Urbana, Illinois 61801, United States;* orcid.org/0000-0001-7360-994X

Complete contact information is available at: https://pubs.acs.org/10.1021/acs.analchem.9b04754

Author Contributions

The manuscript was written through contributions of all authors.

Notes

The authors declare no competing financial interest.

ACKNOWLEDGMENTS

This research was primarily supported by the NSF through the University of Illinois at Urbana−Champaign Materials Research Science and Engineering Center DMR-1720633. Sample characterization was carried out in part in the Materials Research Laboratory Central Research Facilities and Nanotechnology Laboratory, University of Illinois. J.R.L. acknowledges support from the Alfred P. Sloan Research Fellowship. M.J.C thanks Dipobrato Sarbapalli for assistance with graphene transfer and SEM imaging.

REFERENCES

(1) Schorr, N. B.; Hui, J.; Rodríguez-López, J. *Curr. Opin. Electrochem.* **2019**, *13*, 100−106.
(2) Shenoy, G. J.; Parobek, D.; Salim, M.; Li, Z.; Tian, C.; Liu, H. *RSC Adv.* **2016**, *6* (10), 8489−8494.
(3) Wang, Q. H.; Jin, Z.; Kim, K. K.; Hilmer, A. J.; Paulus, G. L. C.; Shih, C.-J.; Ham, M.-H.; Sanchez-Yamagishi, J. D.; Watanabe, K.; Taniguchi, T.; Kong, J.; Jarillo-Herrero, P.; Strano, M. S. *Nat. Chem.* **2012**, *4* (9), 724−732.
(4) González-Herrero, H.; Pou, P.; Lobo-Checa, J.; Fernández-Torre, D.; Craes, F.; Martínez-Galera, A. J.; Ugeda, M. M.; Corso, M.; Ortega, J. E.; Gómez-Rodríguez, J. M.; Perez, R.; Brihuega, I. *ACS Nano* **2016**, *10* (5), 5131−5144.
(5) Sławińska, J.; Zasada, I. *Phys. Rev. B: Condens. Matter Mater. Phys.* **2011**, *84* (23), 235445.
(6) Hui, J.; Zhou, X.; Bhargava, R.; Chinderle, A.; Zhang, J.; Rodríguez-López, J. *Electrochim. Acta* **2016**, *211* (SupplementC), 1016−1023.
(7) Hui, J.; Pakhira, S.; Bhargava, R.; Barton, Z. J.; Zhou, X.; Chinderle, A. J.; Mendoza-Cortes, J. L.; Rodríguez-López, J. *ACS Nano* **2018**, *12* (3), 2980−2990.
(8) Zhang, Y.; Heiranian, M.; Janicek, B.; Budrikis, Z.; Zapperi, S.; Huang, P. Y.; Johnson, H. T.; Aluru, N. R.; Lyding, J. W.; Mason, N. *Nano Lett.* **2018**, *18* (3), 2098−2104.
(9) Nie, S.; Emory, S. R. *Science* **1997**, *275* (5303), 1102−1106.
(10) Zhang, Z.; Kneipp, J. *Anal. Chem.* **2018**, *90* (15), 9199−9205.
(11) Wang, C.; Shi, Y.; Dan, Y.-Y.; Nie, X.-G.; Li, J.; Xia, X.-H. *Chem. - Eur. J.* **2017**, *23* (28), 6717−6723.
(12) Robatjazi, H.; Bahauddin, S. M.; Doiron, C.; Thomann, I. *Nano Lett.* **2015**, *15* (9), 6155−6161.
(13) Seemala, B.; Therrien, A. J.; Lou, M.; Li, K.; Finzel, J. P.; Qi, J.; Nordlander, P.; Christopher, P. *ACS Energy Lett.* **2019**, *4*, 1803−1809.
(14) Zhang, X.; Li, X.; Reish, M. E.; Zhang, D.; Su, N. Q.; Gutiérrez, Y.; Moreno, F.; Yang, W.; Everitt, H. O.; Liu, J. *Nano Lett.* **2018**, *18* (3), 1714−1723.
(15) Wang, C.; Shi, Y.; Yang, D.-R.; Xia, X.-H. *Curr. Opin. Electrochem.* **2018**, *7*, 95−102.
(16) Pu, Y.-C.; Wang, G.; Chang, K.-D.; Ling, Y.; Lin, Y.-K.; Fitzmorris, B. C.; Liu, C.-M.; Lu, X.; Tong, Y.; Zhang, J. Z.; Hsu, Y. J.; Li, Y. *Nano Lett.* **2013**, *13* (8), 3817−3823.

(17) Awazu, K.; Fujimaki, M.; Rockstuhl, C.; Tominaga, J.; Murakami, H.; Ohki, Y.; Yoshida, N.; Watanabe, T. *J. Am. Chem. Soc.* **2008**, *130* (5), 1676−1680.
(18) Huang, X.; Jain, P. K.; El-Sayed, I. H.; El-Sayed, M. A. *Lasers Med. Sci.* **2008**, *23* (3), 217.
(19) Lim, D.-K.; Barhoumi, A.; Wylie, R. G.; Reznor, G.; Langer, R. S.; Kohane, D. S. *Nano Lett.* **2013**, *13* (9), 4075−4079.
(20) Aruda, K. O.; Tagliazucchi, M.; Sweeney, C. M.; Hannah, D. C.; Weiss, E. A. *Phys. Chem. Chem. Phys.* **2013**, *15* (20), 7441−7449.
(21) Wang, C.; Nie, X.-G.; Shi, Y.; Zhou, Y.; Xu, J.-J.; Xia, X.-H.; Chen, H.-Y. *ACS Nano* **2017**, *11* (6), 5897−5905.
(22) Zhou, L.; Swearer, D. F.; Zhang, C.; Robatjazi, H.; Zhao, H.; Henderson, L.; Dong, L.; Christopher, P.; Carter, E. A.; Nordlander, P.; Halas, N. J. *Science* **2018**, *362* (6410), 69−72.
(23) Golubev, A. A.; Khlebtsov, B. N.; Rodriguez, R. D.; Chen, Y.; Zahn, D. R. T. *J. Phys. Chem. C* **2018**, *122* (10), 5657−5663.
(24) Keller, E. L.; Frontiera, R. R. *ACS Nano* **2018**, *12* (6), 5848−5855.
(25) Yu, Y.; Sundaresan, V.; Willets, K. A. *J. Phys. Chem. C* **2018**, *122* (9), 5040−5048.
(26) Yu, Y.; Williams, J. D.; Willets, K. A. *Faraday Discuss.* **2018**, *210* (0), 29−39.
(27) Schorr, N. B.; Jiang, A. G.; Rodríguez-López, J. *Anal. Chem.* **2018**, *90* (13), 7848−7854.
(28) Simpson, B. H.; Rodríguez-López, J. *J. Am. Chem. Soc.* **2015**, *137* (47), 14865−14868.
(29) Zhao, Z.; Leonard, K. C.; Boika, A. *Anal. Chem.* **2019**, *91* (4), 2970−2977.
(30) Bukola, S.; Liang, Y.; Korzeniewski, C.; Harris, J.; Creager, S. *J. Am. Chem. Soc.* **2018**, *140* (5), 1743−1752.
(31) Bukola, S.; Beard, K.; Korzeniewski, C.; Harris, J. M.; Creager, S. E. *ACS Appl. Nano Mater.* **2019**, *2* (2), 964−974.
(32) Mogg, L.; Zhang, S.; Hao, G.-P.; Gopinadhan, K.; Barry, D.; Liu, B. L.; Cheng, H. M.; Geim, A. K.; Lozada-Hidalgo, M. *Nat. Commun.* **2019**, *10* (1), 1−5.
(33) Polcari, D.; Dauphin-Ducharme, P.; Mauzeroll, J. *Chem. Rev.* **2016**, *116* (22), 13234−13278.
(34) Ritzert, N. L.; Rodríguez-López, J.; Tan, C.; Abruña, H. D. *Langmuir* **2013**, *29* (5), 1683−1694.
(35) Lefrou, C.; Cornut, R. *ChemPhysChem* **2010**, *11* (3), 547−556.
(36) Baffou, G.; Berto, P.; Bermúdez Ureña, E.; Quidant, R.; Monneret, S.; Polleux, J.; Rigneault, H. *ACS Nano* **2013**, *7* (8), 6478−6488.
(37) Sánchez-Sánchez, C. M.; Bard, A. J. *Anal. Chem.* **2009**, *81* (19), 8094−8100.
(38) Fang, Z.; Wang, Y.; Liu, Z.; Schlather, A.; Ajayan, P. M.; Koppens, F. H. L.; Nordlander, P.; Halas, N. J. *ACS Nano* **2012**, *6* (11), 10222−10228.
(39) Sharma, M.; Jang, J.-H.; Shin, D. Y.; Kwon, J. A.; Lim, D.-H.; Choi, D.; Sung, H.; Jang, J.; Lee, S.-Y.; Lee, K. Y.; Park, H.-Y.; Jung, N.; Yoo, S.-J. *Energy Environ. Sci.* **2019**, *12* (7), 2200−2211.
(40) Papavinasam, S. Electrochemical Polarization Techniques for Corrosion Monitoring. In *Techniques for Corrosion Monitoring*; Elsevier, 2008; pp 49−85. DOI: 10.1533/9781845694050.1.49.
(41) Shi, F.; He, J.; Zhang, B.; Peng, J.; Ma, Y.; Chen, W.; Li, F.; Qin, Y.; Liu, Y.; Shang, W.; Tao, P.; Song, C.; Deng, T.; Qian, X.; Ye, J.; Wu, J. *Nano Lett.* **2019**, *19* (2), 1371−1378.
(42) Schmidt, T. J.; Stamenkovic, V.; Ross, Jr., P. N.; Markovic, N. M. Temperature Dependent Surface Electrochemistry on Pt Single Crystals in Alkaline Electrolyte: Part 3: The Oxygen Reduction Reaction. *Phys. Chem. Chem. Phys.* 2003, *5*, 400−406; .
(43) Bard, A. J.; Faulkner, L. R. In *Electrochemical Methods Fundamentals and Applications*; John Wiley & Sons, Inc., 2001; pp 199−200.
(44) Laidler, K. J. *J. Chem. Educ.* **1984**, *61* (6), 494.
(45) Pimenta, M. A.; Dresselhaus, G.; Dresselhaus, M. S.; Cançado, L. G.; Jorio, A.; Saito, R. *Phys. Chem. Chem. Phys.* **2007**, *9* (11), 1276−1290.
(46) Kim, M.; Lin, M.; Son, J.; Xu, H.; Nam, J.-M. *Adv. Opt. Mater.* **2017**, *5* (15), 1700004.
(47) Narang, P.; Sundararaman, R.; Atwater, H. A. Plasmonic Hot Carrier Dynamics in Solid-State and Chemical Systems for Energy Conversion. *Nanophotonics* **2016**, *5* (1). DOI: 10.1515/nanoph-2016-0007.
(48) Chen, K.; Yogeesh, M. N.; Huang, Y.; Zhang, S.; He, F.; Meng, X.; Fang, S.; Sheehan, N.; Tao, T. H.; Bank, S. R.; Lin, J. F.; Akinwande, D.; Sutter, P.; Lai, T.; Wang, Y. *Carbon* **2016**, *107*, 233−239.
(49) Estrada, D.; Li, Z.; Choi, G.-M.; Dunham, S. N.; Serov, A.; Lee, J.; Meng, Y.; Lian, F.; Wang, N. C.; Perez, A.; Haasch, R. T.; Zuo, J.-M.; King, W. P.; Rodgers, J. A.; Cahill, D. G.; Pop, E. *Npj 2D Mater. Appl.* **2019**, *3* (1), 10.
(50) Brownson, D. A. C.; Varey, S. A.; Hussain, F.; Haigh, S. J.; Banks, C. E. *Nanoscale* **2014**, *6* (3), 1607−1621.

https://dx.doi.org/10.1021/acs.analchem.9b04754
Anal. Chem. 2020, 92, 3666−3673